JGR Solid Earth

RESEARCH ARTICLE
10.1029/2025JB033147

Key Points:
- Dense-array ambient noise autocorrelation images three laterally continuous crustal reflectors beneath northern Taiwan
- The reflectors delineate a Moho, a Moho-parallel reflective band in the lowermost crust, and a gently dipping mid-crustal interface
- The mapped reflector constrain crustal architecture and deformation, suggesting vertically partitioned deformation

Supporting Information:
Supporting Information may be found in the online version of this article.

Correspondence to:
M. Chien,
mc132@rice.edu

Citation:
Chien, M., Levander, A., & Chen, P.-F. (2026). Autocorrelation seismic imaging of northern Taiwan using ambient noise data. *Journal of Geophysical Research: Solid Earth*, *131*, e2025JB033147. https://doi.org/10.1029/2025JB033147

Received 7 OCT 2025
Accepted 30 APR 2026

Author Contributions:
Conceptualization: Mei Chien, Alan Levander
Data curation: Mei Chien, Alan Levander, Po-Fei Chen
Formal analysis: Mei Chien, Alan Levander
Funding acquisition: Alan Levander
Investigation: Mei Chien, Alan Levander
Methodology: Mei Chien, Alan Levander
Project administration: Mei Chien, Alan Levander
Resources: Mei Chien, Alan Levander, Po-Fei Chen
Software: Mei Chien, Alan Levander
Supervision: Mei Chien, Alan Levander, Po-Fei Chen
Validation: Mei Chien, Alan Levander
Visualization: Mei Chien, Alan Levander

Autocorrelation Seismic Imaging of Northern Taiwan Using Ambient Noise Data

Mei Chien[1], Alan Levander[1], and Po-Fei Chen[2]

[1]Department of Earth, Environmental, and Planetary Sciences, Rice University, Houston, TX, USA, [2]Department of Earth Sciences, National Central University, Taoyuan, Taiwan

Abstract Over the past few million years, northern Taiwan records a tectonic history of subduction to arc–continent collision followed by post-collisional collapse. This evolution motivates constraints on crustal structure, including crustal layering and thickness. We analyze 7 months of continuous vertical-component recordings from the dense Formosa Array and retrieve zero-offset P-wave reflectivity using ambient noise autocorrelation. Stacked autocorrelation functions image three laterally persistent positive polarity arrivals beneath northern Taiwan. The deepest arrival is interpreted as the Moho (PmP) at 11–15 s two-way travel time (TWT), corresponding to depths of ∼30–47 km. The Moho deepens beneath the mountain belt and shallows toward the Ilan Plain. A second reflector occurs, on average, ∼5 km above the Moho and forms a laterally continuous, Moho-parallel band in the lowermost crust. A shallow intracrustal reflector lies at 5–8 s TWT (∼12–22 km depth) and dips gently to the east–southeast; crustal seismicity is predominantly located above this interface. Synthetic modeling and depth-conversion sensitivity tests indicate that the principal arrivals are robust and that depth uncertainties are modest. These observations provide new constraints on crustal layering and interface geometry beneath northern Taiwan derived from dense-array ambient-noise reflectivity imaging.

Plain Language Summary We used seismic noise to make images of the crust beneath northern Taiwan. Instead of analyzing explosions or earthquakes, we listened continuously for 7 months and processed background noise signals to find echoes from deep boundaries. Our results show three main features. First, the crust–mantle boundary gets deeper from north to south, from about 30 to 47 km. Second, we detect a reflective layer a few kilometers above the crust–mantle boundary, which likely represents a distinct lowermost crustal layer that formed during an earlier rifting stage in the South China Sea, before Taiwan's mountain building. Third, we see a gentle east–southeast dipping surface at depths of roughly 12–22 km in the upper to middle crust. This surface is likely a detachment fault, a boundary separating two layers that deform in different ways. These findings provide a clearer picture of how ambient noise imaging can help test tectonic models in similar mountain belts.

1. Introduction

1.1. Tectonic Framework

Taiwan is a young mountain belt (∼4–6 Myr) formed by ongoing arc–continent collision and associated active tectonics. Its tectonic evolution began with rifting of the South China Sea (∼30 Ma) and later evolved into collision between the Philippine Sea Plate–Luzon Arc system and the Eurasian continental passive margin (Lin et al., 2003). Presently, the Philippine Sea Plate and the Eurasian Plate converge at ∼80 mm/yr in a NW–SE direction (Yu et al., 1997), producing an oblique collision that propagates from northeast to southwest (Suppe, 1984; Teng, 1990). South of Taiwan and offshore, South China Sea oceanic lithosphere subducts beneath the Philippine Sea Plate; in central Taiwan, oceanic lithosphere has largely been consumed and collision involves the Eurasian continental crust and Luzon Arc.

Northern Taiwan differs from the active collision zone. Near ∼24.5°N, where the orogenic strike shifts from NNE–SSW to NE–SW, arc–continent collision has waned and subduction polarity has reversed, with the Philippine Sea Plate now subducting northwestward beneath the Eurasian Plate. As a result, previously uplifted northern Taiwan is undergoing post-collisional extension and collapse, expressed by reduced relief, extensional structures (e.g., the Sanchiao Fault and the Taipei Basin), Ryukyu arc andesites overlying older orogenic strata, shallow extensional focal mechanisms (Teng, 1996), and clockwise rotation relative to Penghu inferred from GPS

Writing – original draft: Mei Chien
Writing – review & editing: Mei Chien, Alan Levander

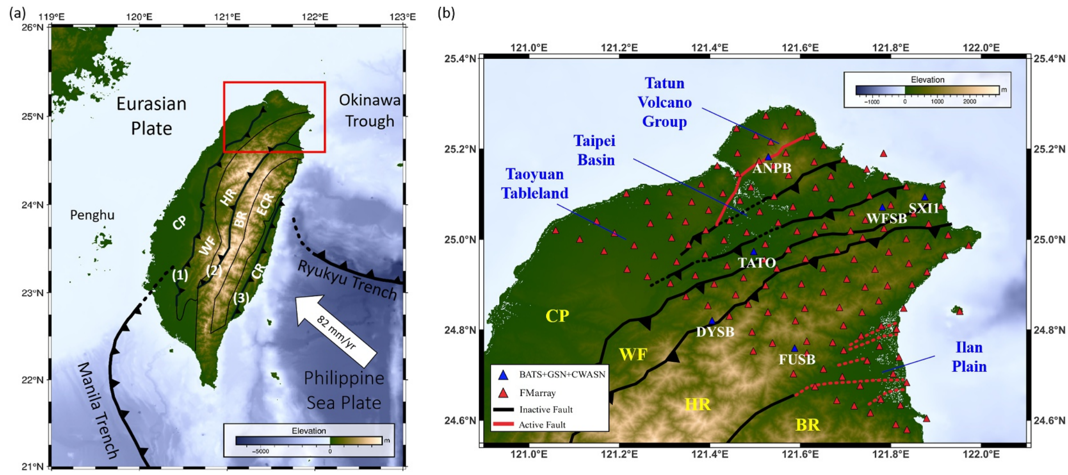

Figure 1. (a) Tectonic setting of Taiwan: The white arrow indicates the plate-motion direction and rate based on GPS measurements (Yu et al., 1997). Surface geological units are from Wu et al. (2014): CP = Coastal Plain, WF = Western Foothills, HR = Hsueshan Range, BR = Backbone Range, ECR = Eastern Central Range, CR = Coastal Range. (1) Chukou Thrust-Chelungpu-Sani Thrust; (2) Lishan Fault; (3) Longitudinal Valley Fault. (b) Red box in (a): Red triangles represent Formosa Array stations; blue triangles denote BATS and CWASN stations used in this study. Fault traces from Liu et al. (2021) are shown in black and red. The red solid line represents the active Sanchiao Fault. Black lines with triangles indicate inactive thrust faults; from west to east these are the Kanjiao Fault, Taipei Fault, Hsintien Fault, and Chuchih Fault. The red dashed lines represent active blind faults.

velocities (Tsai et al., 2015; Figure 1a). Because northern Taiwan may represent a later stage of the orogenic cycle, its present structure provides clues to the future evolution of central and southern Taiwan.

1.2. Geological Setting

Geologically, Taiwan is composed of NNE-trending terrane belts emplaced during collision between the Luzon Arc and the Eurasian continental margin, and these belts are arranged broadly transverse to the convergence direction. From east to west, the major geological units are the Coastal Range, Central Range (Eastern Central Range and Backbone Range), Hsueshan Range, Western Foothills, and Coastal Plain (Figure 1a). The Coastal Range, formerly part of the Luzon Arc, is dominated by forearc and arc-related volcanic rocks. West of the Coastal Range, the Longitudinal Valley Fault marks the suture zone between the Philippine Sea Plate and the Eurasian Plate. Units west of this suture zone represent the Eurasian passive margin and show a westward decrease in metamorphic grade away from the suture. The Eastern Central Range exposes a pre-Tertiary metamorphic basement complex interpreted as former continental slope material, whereas the Backbone Range consists of metamorphic basement overlain by Cenozoic argillaceous strata of the former continental shelf. The Lishan Fault separates the Central Range from the Hsueshan Range, which also derives from the former shelf but is less metamorphosed (argillite–slate belt). The Western Foothills comprise Eocene–Pleistocene clastic sediments of the foreland basin deformed into a fold-and-thrust belt dominated by low-angle thrusts. The Coastal Plain overlies the foreland basin fill of alluvial sediments and clastic deposits (Ho, 1986; Lin & Watts, 2002).

1.3. Tectonic Evolution Models

Multiple models have been proposed to explain the orogenic evolution of Taiwan. Suppe (1981) proposed a thin-skinned model in which Taiwan forms an accretionary wedge of passive-margin sediments and upper-crustal units that deform above a basal décollement. This décollement separates the overlying wedge from the underthrusting Eurasian Plate, with the Luzon Arc acting as the backstop. In contrast, Wu et al. (1997) proposed a lithospheric-collision model in which deformation is distributed throughout the Eurasian lithosphere, implying lithospheric-scale shortening rather than slip localized on a single décollement. These end-member models differ primarily in the depth extent of deformation and the presence of a basal detachment, and several intermediate or derivative models have been proposed. For example, Huang et al. (2015) suggested a two-layer model involving depth-dependent anisotropy and inferred mechanical behavior, with the upper layer dominated by compression and the lower layer by shearing. Taken together, the proposed models span a range of deformation styles rather than a single binary choice; in many fold-and-thrust belts, deformation reflects a combination of thin- and thick-skinned mechanisms (Nemčok et al., 2013; Schlunegger & Kissling, 2015; Wissinger et al., 1998). Distinguishing among these models requires constraints on crustal and upper mantle geometry from seismic imaging, including the internal structure of the thrust belt, the depth and continuity of detachment surfaces, lateral variation in crustal thickness, and the geometry and extent of any underthrust or subducted Eurasian lithosphere.

1.4. Crustal Imaging Techniques

Previous crustal imaging studies in Taiwan have used earthquake tomography (Huang et al., 2014; Kuo-Chen et al., 2012; Ustaszewski et al., 2012), seismic refraction and reflection (Kuo et al., 2016; McIntosh et al., 2005; Van Avendonk et al., 2016), gravity anomalies (Hsieh & Yen, 2016), ambient noise interferometry for shear wave velocities (Ai et al., 2019; Huang et al., 2015; Liu et al., 2021), and receiver functions (Chi et al., 2022; Goyal & Hung, 2021; Kim et al., 2004; Wang et al., 2010). Many of these studies used dense linear arrays (e.g., the TAIGER project; Kuo-Chen et al., 2012) and permanent broadband stations, such as the Broadband Array in Taiwan for Seismology (BATS) operated by the Institute of Earth Sciences, Academia Sinica (IES). Even so, published estimates of maximum crustal thickness in central Taiwan range from ∼50 to 60 km (Kuo-Chen et al., 2012; Wu et al., 1997, 2007).

This variability partly reflects differences in what each method resolves and how the Moho is defined. Seismic tomography is typically smooth and emphasizes gradual velocity variations, and the Moho is commonly inferred from velocity isosurfaces. In contrast, controlled-source experiments, receiver functions, and autocorrelation functions can better resolve sharp impedance contrasts at discontinuities such as the Moho. However, controlled-source surveys are constrained by station spacing, aperture, and shot density due to the associated costs. Receiver functions estimate interface depths from travel-time differences of converted phases (Ammon, 1991; Langston, 1979), but traditional receiver-function applications rely on teleseismic earthquakes that are often unevenly distributed in azimuth. Related earthquake-based autocorrelation approaches, including teleseismic P-wave coda autocorrelation, can also image crustal discontinuities, although they likewise depend on earthquake occurrence and source distribution. By comparison, ambient noise sources are spatially widespread and continuous in time, making them an excellent resource for subsurface imaging.

Because ambient noise imaging still benefits from dense station coverage, the Formosa Array (FA) provides an opportunity to map reflectivity at higher spatial resolution than is available from permanent networks. In 2017, the Institute of Earth Sciences (IES) deployed the FA, a dense broadband seismic array in northern Taiwan (Figure 1b). The FA comprises 146 stations equipped with Nanometrics Meridian Compact PH sensors and spaced at ∼5 km intervals. Using ambient noise autocorrelations, we retrieve the zero-offset reflection response beneath each station and construct autocorrelation-based reflectivity images across northern Taiwan. These images delineate laterally variable crustal interfaces, including the Moho and prominent intracrustal reflectors, which we interpret in the context of active mountain building and potential detachment-related deformation. We assess the robustness of the inferred interfaces through processing-stability tests, synthetic tests, and comparisons with independent constraints from regional studies.

2. Methodology and Data

2.1. Seismic Interferometry

Seismic interferometry uses correlations between receivers to estimate a virtual seismic Green's function (Wapenaar et al., 2010). As the distance between two stations decreases and eventually converges to a single point, cross-correlation becomes autocorrelation. Claerbout (1968) showed that autocorrelating the surface recording of a vertically transmitted plane wave in a one-dimensional medium yields the zero-offset reflection response of the subsurface. This concept was later extended to elastic waves at non-normal incidence (Frasier, 1970), to three-dimensional media (Wapenaar et al., 2008), and further developed for correlation imaging in exploration settings (Schuster, 2009). Over the past few decades, ambient noise autocorrelation has been used to retrieve P-wave reflections from basement interfaces (Romero & Schimmel, 2018) and the crust–mantle boundary in relatively homogeneous continental settings (Gomez-Garcia et al., 2023; Gorbatov et al., 2013; Kennett et al., 2015; Oren & Nowack, 2017), as well as in laterally heterogeneous environments including subduction zones (Ashruf & Morelli, 2022; Ito et al., 2012) and volcanic regions (Heath et al., 2018). Related autocorrelation approaches based on local and teleseismic earthquake wavefields, including teleseismic P-wave

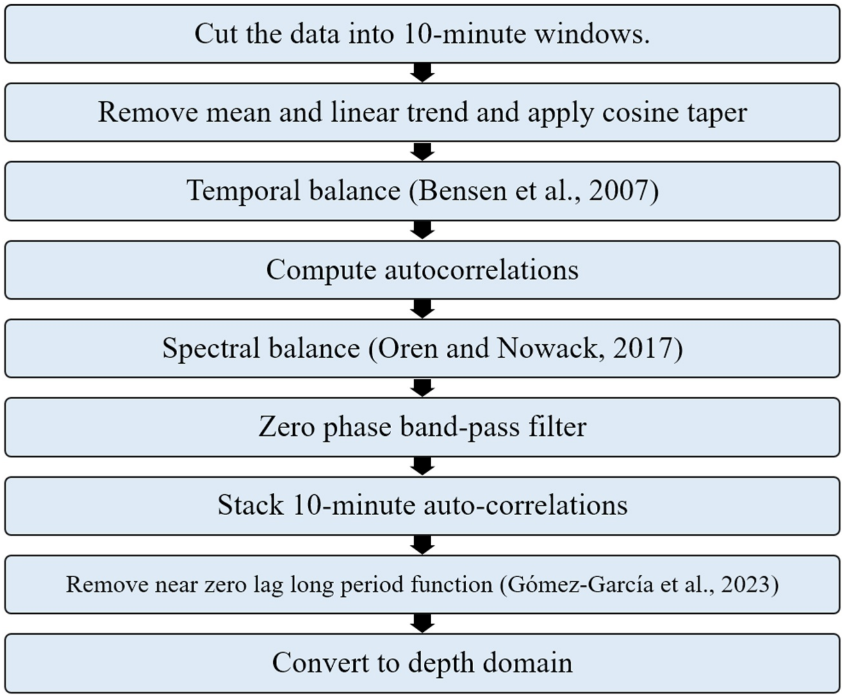

Figure 2. Processing workflow used in this study.

coda autocorrelation, have also been used to image crustal and uppermost mantle discontinuities in a range of tectonic settings (e.g., Alemayehu et al., 2023; Ouammou et al., 2026; Phạm & Tkalčić, 2018; Thapa & Vlahovic, 2025; Thapa et al., 2023). Because autocorrelation-based methods can provide reflection constraints with limited aperture, it is well suited to short station deployments and sparse networks, and has been applied to planetary seismology (Deng & Levander, 2020, 2023). In this study, we use stacked vertical-component autocorrelations as a first-order approximation to the zero-offset P-wave reflection response beneath each station and interpret coherent arrivals as reflectivity from major impedance contrasts.

2.2. Data

We analyzed seven months of continuous vertical-component waveforms recorded by the Formosa Array in northern Taiwan (August 2019–February 2020), sampled at 20 Hz and recorded by stations spaced at ~5 km. To provide an independent comparison using permanent broadband stations overlapping the FA footprint, we included (a) four stations from the Broadband Array in Taiwan for Seismology (BATS; FDSN network code TW): DYSB, FUSB, SXI1, and WFSB; (b) station TATO from the IRIS/USGS Global Seismograph Network (FDSN network code IU); and (c) station ANP from the Central Weather Administration Seismographic Network (CWASN; FDSN network code T5). All comparison stations were analyzed over the same time window as the FA. All TW and IU waveforms were obtained via BATS Web Services, and T5 waveforms were obtained via the Seismological and Geophysical Data Management System (GDMS) of the Central Weather Administration. The TW and IU data are archived at 20 Hz, matching the FA sampling rate, whereas ANP is available as a higher-sample-rate vertical channel (HHZ). We applied the same preprocessing and autocorrelation workflow to all data sets to ensure consistency.

Earthquake hypocenters were obtained from the CWA GDMS catalog (1973-01-01–2024-08-12) for regional context and seismicity mapping. We used the routine catalog locations without independent relocation and selected events within the study region. For quality control, we retained only earthquakes with reported epicentral standard error ≤5 km and depth standard error ≤5 km.

2.3. Workflow

The processing workflow is summarized in Figure 2. We first segmented the continuous records into 10-min windows and discarded windows that were entirely zero or in which ≥95% of samples were zero, indicating gaps or missing samples. For the remaining windows, we removed the mean and linear trend and applied a cosine taper. We did not remove the instrument response because the broadband response is approximately flat in velocity over the target frequency band used here.

Local earthquakes and other transient signals can dominate correlations and obscure the ambient noise reflection response. To reduce their influence, we applied temporal normalization using a running absolute-mean method with a 60-s window (Bensen et al., 2007). We then autocorrelated each 10-min window to obtain an autocorrelation function (ACF). For analysis and display, we retained the causal (non-negative) part.

Following Oren and Nowack (2017), we applied spectral-division whitening to each temporally normalized 10-min ACF prior to stacking. Specifically, we divided the ACF spectrum by the amplitude spectrum of the same ACF windowed around zero lag (cosine-tapered window spanning ±10 s). To stabilize the division and prevent amplification where the denominator spectrum is very small, we used a water level equal to 1% of the maximum spectral amplitude, which provided a stable whitening result while preserving the main waveform characteristics.

After testing several filter ranges, we selected a zero-phase 0.1–1 Hz bandpass filter because it produced the most consistent reflector character across stations and allowed the subsequent long-period trend to be fit and removed most effectively. We then stacked the causal ACFs for each station to improve signal-to-noise, using ~23,000 10-min windows per station on average. Because our processed ACFs are band-limited, the zero-lag peak is broadened and accompanied by oscillatory sidelobes that extend into short times near zero-lag, producing a low-frequency baseline that can mask weak crustal reflections. To prevent the dominant central peak and its sidelobes from controlling subsequent processing, we set the 0–3 s portion of each station-stacked ACF to zero.

Following Gómez-García et al. (2023), we estimated and removed the residual baseline by fitting a smooth long-period function (a slowly varying baseline with lag time) to each station stack over 3–30 s and subtracting the fitted curve:

$$y = de^{-\alpha t}\cos(\omega_1 \mathrm{t} + \varphi_1) + g\cos(\omega_2 t + \varphi_2) \tag{1}$$

where t is lag time, α is the exponential decay constant, ω_1 and ω_2 are angular frequencies, φ_1 and φ_2 are phase delays, and d and g are the amplitudes of the first and second cosine terms, respectively. The first term represents a decaying oscillatory component associated with the broadened zero-lag peak, whereas the second term accounts for a lower-frequency oscillation of approximately constant amplitude at longer lag times. The seven parameters were estimated iteratively until the coefficient of determination reached $R^2 = 0.95$. The lower bound (3 s) matches the 0–3 s mute and avoids the interval dominated by the broadened zero-lag peak and sidelobes, while the upper bound (30 s) provides a sufficiently long window to stabilize the estimate while remaining within the lag range used to interpret crustal reflections. Figure 3a shows an example of the fitted long-period function superimposed on the stacked ACF, and Figure 3b shows the residual ACF after subtracting the fitted function from the stacked ACF.

To convert the ACFs from time to depth, we constructed station-specific 1-D P-wave velocity models. For each station, we extracted 1-D Vp(z) profiles from published models (Huang et al., 2014; Kim et al., 2005; Kuo-Chen et al., 2012; Kuo et al., 2016; Wu et al., 2009) at the station location and interpolated them onto a common depth grid. We defined a representative station model by averaging the Vp(z) ensemble (red curve in Figure 4b). To account for low-velocity basin structures in the upper crust, we replaced the shallow portion of each station's 1-D profile (≤5 km) with the Vp converted from the shear-wave velocity model of Huang et al. (2021) using a constant Vp/Vs ratio. We adopt Vp/Vs = 1.728, consistent with the Wadati-diagram constraint used by Huang et al. (2014) and within the range inferred for northern Taiwan (Vp/Vs ≈ 1.70–1.73; Lin et al., 2016). Using these final station-specific models, we converted stacked ACFs from two-way time to depth.

Finally, we manually picked reflector lag times on stacked ACF sections by tracking laterally continuous negative-amplitude troughs along each cross-section. In vertical-component autocorrelations, a negative ACF amplitude corresponds to a positive P-wave reflection polarity, which we refer to as a positive polarity. Where

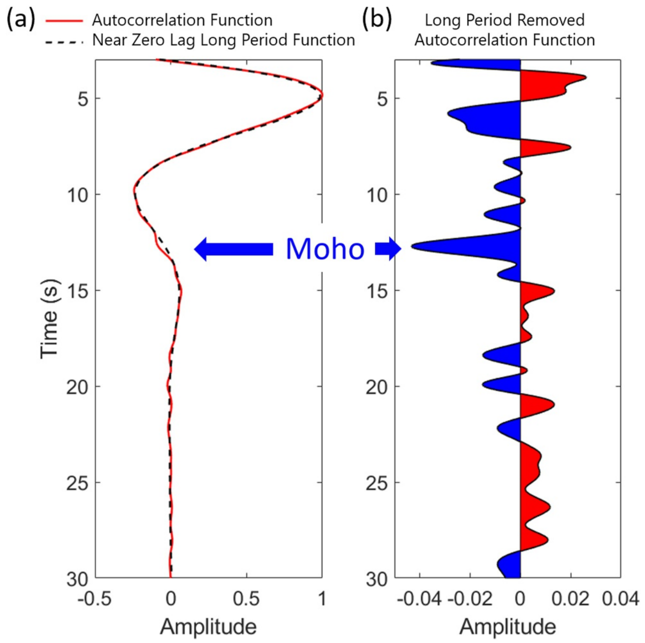

Figure 3. (a) Seven-month stacked autocorrelation function (ACF) for representative station CT16. The fitted long-period function in lag time (black dashed line; Equation 1) is shown after 0.1–1 Hz bandpass filtering and stacking. (b) Residual ACF obtained after subtracting the estimated long-period function from the stacked ACF.

arrivals exhibited closely spaced minima, we selected the branch that was most laterally coherent and cross-checked consistency between adjacent profiles and between time and depth views (Text S1 in Supporting Information S1). Thus, pick position was defined by the trough minimum, whereas reflector identification was based on phase polarity, lag-time window, lateral continuity, consistency after time-to-depth conversion, and comparison with the synthetic tests in Section 3.2.

2.4. ACF Stability

To evaluate ACF stack convergence and to reduce the likelihood that non-stationary noise sources bias the stacks, we performed the stability test of Gómez-García et al. (2023). For each station, we computed the Pearson correlation coefficient between the final stacked ACF and the cumulative stack formed by progressively adding 10-min ACF windows. Figure 5 summarizes the resulting correlation trajectories for all stations, together with the array median, mean, and ±1σ envelope. Most stations reach high similarity within the first several thousand windows. Stations KM28 and KE17 converge much more slowly than the rest of the array, requiring >15,000 windows (≈4 months of continuous recording) to reach a correlation coefficient of 0.99; both stations also have frequent recording gaps. We therefore exclude them from further analysis. Five additional stations (KM16, KM29, KM34, PN19, and CT15) have insufficient or no usable data and are also excluded. After these removals, the mean number of windows required to reach a correlation coefficient of 0.99 is 1,064 (≈8 days of continuous data). Because the average station stack in this study contains ~23,000 windows, ~15 times the minimum for a stable stacked trace, we conclude that the main reflector arrivals identified in the stacked ACFs are stable and reproducible.

To assess whether the ambient noise wavefield provides sufficiently broad illumination for autocorrelation imaging, we performed array beamforming on the continuous records (Text S2 and Figure S1 in Supporting Information S1). The results show that background-noise energy is typically distributed across multiple azimuths and slownesses, supporting the use of the 7-month data set. A more detailed beamforming analysis is presented elsewhere (Chien et al., submitted).

3. Results

3.1. Crustal Reflectivity Imaged by Autocorrelation Functions

Stacked vertical-component ACFs reveal three laterally persistent positive P-wave arrivals (negative ACF amplitude) across the Formosa Array profiles (Figure 6). The deepest arrival (magenta marks) is interpreted as the Moho P-wave reflection (PmP), appearing at 11–15 s TWT and corresponding to depths of 30–47 km. Across the Formosa Array, the inferred depth to Moho increases from ~30 km near the northern edge of Taiwan to ~47 km beneath the southern part of the array, with an average depth of ~39 km (Figure 7a). The Moho is deepest (>42 km) beneath the fold-and-thrust belt, including the Hsueshan Range and the Western Foothills, and shallows to ~38 km beneath the Ilan Plain.

A second-deepest arrival (red marks; Reflector 1) occurs at 10–13 s TWT (28–40 km). It marks the onset of a sequence of pulses with the same polarity as the primary Moho arrival and lies, on average, ~5 km above the Moho ($1\sigma = 1.6$ km). The separation between Reflector 1 and the Moho ranges from 1.9 to 10 km across the array (0.5–2.6 s TWT; Figures 7b and 7d).

A shallower intracrustal arrival (blue marks; Reflector 2) occurs at 5–8 s TWT (12–22 km) and dips ~3°–7° to the east–southeast (Figures 7c and 8). Seismicity is predominantly located above Reflector 2 (Figure 8). Several profiles also show intermittent shallow negative troughs at ~3–6 s (4–10 km) above Reflector 2; because these are not laterally continuous, we treat them as localized shallow structure rather than a region-wide interface. ACF waveforms become more complex beneath the Western Foothills and Hsueshan Range, where multiple pulses are

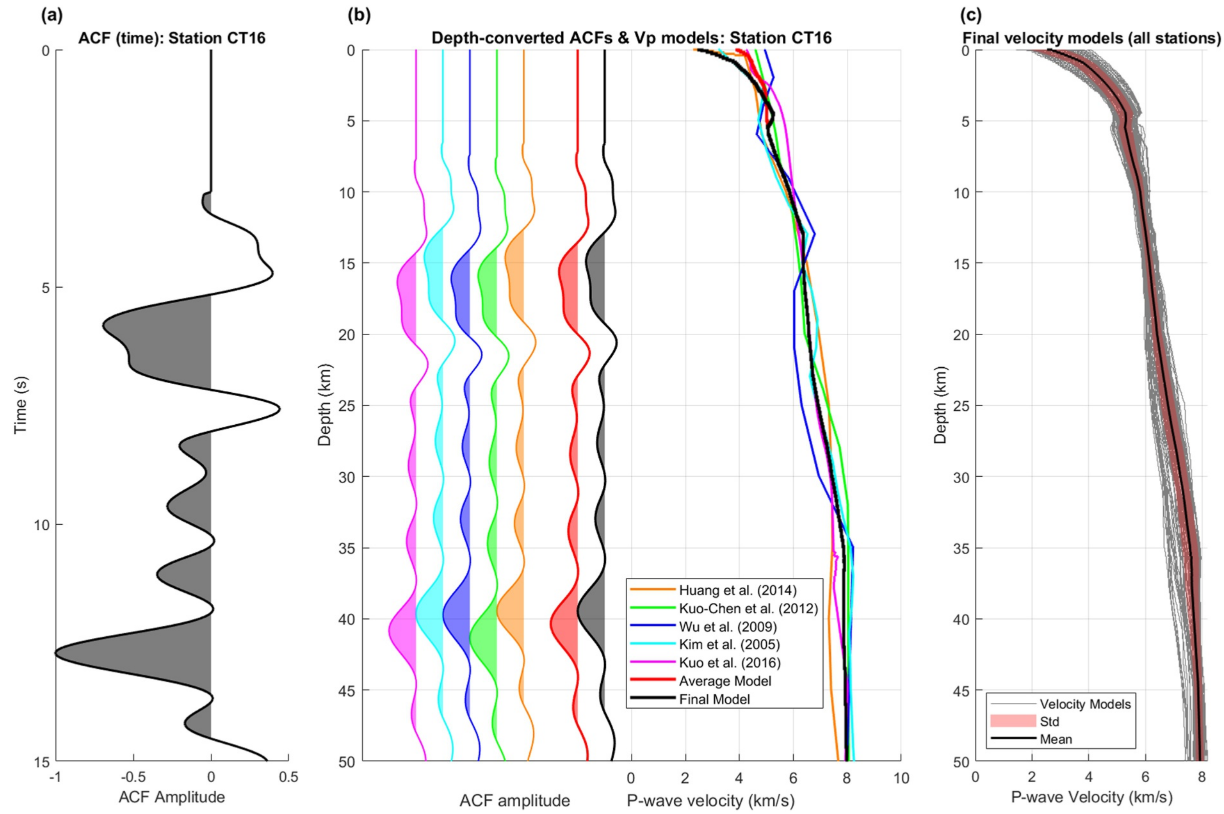

Figure 4. Autocorrelation functions for reference station CT16 and the corresponding P-wave velocity models. (a) Autocorrelation function in the time domain. (b) Depth-converted ACF based on the corresponding velocity models, using the same color scheme. The average model (red line) is the mean of the candidate Vp(z) profiles used for time-to-depth conversion. The final model (black line) matches the average model below 5 km depth but replaces the shallow section (≤5 km) with Vp converted from the shear-wave velocity model of Huang et al. (2021) (see text for details). (c) Gray lines show the final velocity models for all stations; the black line shows the across-station mean, and the red shaded area indicates ±1 standard deviation.

observed (Figures 6 and 8), consistent with increased structural complexity in that region. The later signal near ~8 s is most evident within this more complex mountain-belt wavefield and is therefore not interpreted as a separate laterally continuous regional reflector.

The lateral continuity of these arrivals across the profiles indicates that they represent common crustal features. Depth uncertainty arises from two sources: (a) uncertainty in the published crustal Vp models used for time–depth conversion and (b) uncertainty in the shallowest velocity structure ($z < z1$) introduced by the assumed Vp/Vs used to convert the shallow Vs model to Vp. Examining all stations, the median 1σ depth uncertainty associated with the choice of published Vp models is ≤2.1 km (largest at the Moho), whereas varying the assumed shallow Vp/Vs from 1.70 to 1.80 produces a Moho depth shift of −0.184 to +0.448 km (i.e., ≤0.45 km) (Text S3 in Supporting Information S1). Next, we evaluate the timing, interference, and resolvability of the identified reflection arrivals using 1-D synthetic tests (Section 3.2).

3.2. Synthetic Test

We use 1-D synthetics to relate a layered velocity structure to the ACF response and to guide interpretation of the observed arrivals. The tests are designed to (a) confirm that a simple layered model reproduces the principal reflection times and waveform character, (b) evaluate resolvability of closely spaced interfaces, and (c) identify lag-time windows where shallow multiples may overlap primary reflections. We compute the vertical-incidence plane-wave P-SV response of a horizontally layered medium using the Haskell propagator-matrix method (Aki & Richards, 1980). For these tests we assume the incidence angle $\theta = 0°$ ($p = 0$ s/km). The formulation yields the vertical surface displacement response. We apply a zero-phase wavelet to the displacement Green's function and

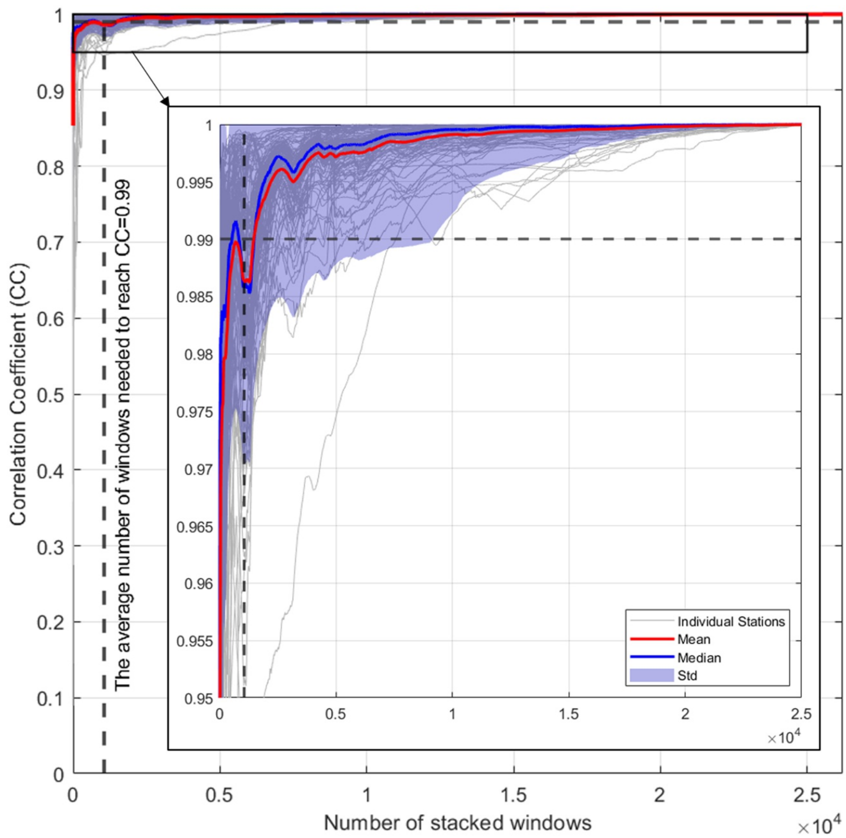

Figure 5. Stability test used to determine the number of windows required to produce a stable ACF. At stacking iteration k, the kth time-domain autocorrelation function is correlated with the cumulative stack of the previous $k - 1$ ACFs, and the correlation coefficient is computed. Gray lines show results for individual stations. The red and blue lines show the mean and median across stations (excluding discarded stations), and the shaded envelope indicates $\pm 1\sigma$ about the mean. The vertical dashed line marks the average number of windows (1,064) required to achieve a coefficient of 0.99, and the horizontal dashed line marks 0.99.

then differentiate to obtain vertical velocity. We then autocorrelate the velocity time series so the synthetic ACFs are directly comparable to the observed vertical-velocity ACFs.

The reference model (Figures 9a–9c) contains interfaces at 7, 15, 33, and 37 km, corresponding to a shallow interface, Reflector 2, Reflector 1, and the Moho, respectively. Layer velocities are taken from the station-average 1-D models used for time-to-depth conversion (Text S4 in Supporting Information S1). S-wave velocities are computed using a constant Vp/Vs ratio, and densities follow an empirical Vp–ρ relationship (Gardner et al., 1974). Red dashed lines in Figure 9 mark the predicted PP two-way travel times to each interface and align with the main synthetic ACF wave packets at the corresponding lag times, supporting interpretation of the observed arrivals as reflections from layered discontinuities rather than multiples.

Wavelet bandwidth strongly controls temporal resolvability. With a 1-Hz Ricker wavelet (Figure 9a), the auto-correlation lobes are narrow enough that Reflector 1 and the Moho, separated by ~1 s in two-way time, remain distinguishable. With a 0.25-Hz Ricker wavelet (Figure 9b), broader wave packets increase overlap and can merge closely spaced arrivals, reducing separation of Reflector 1 from the Moho at low frequency. These tests indicate that, where interfaces are closely spaced in lag time, observed ACF arrivals may appear broadened or partially merged; therefore, reflector assignment in such areas relies on continuity across neighboring stations and adjacent profiles rather than on a single trace alone. The synthetics also highlight a potential ambiguity near ~6 s, where the PP reflection from the 15-km interface falls close to early shallow reverberations associated with the 7-km interface. As a result, energy in this window can include both primary and reverberatory contributions.

10.1029/2025JB033147

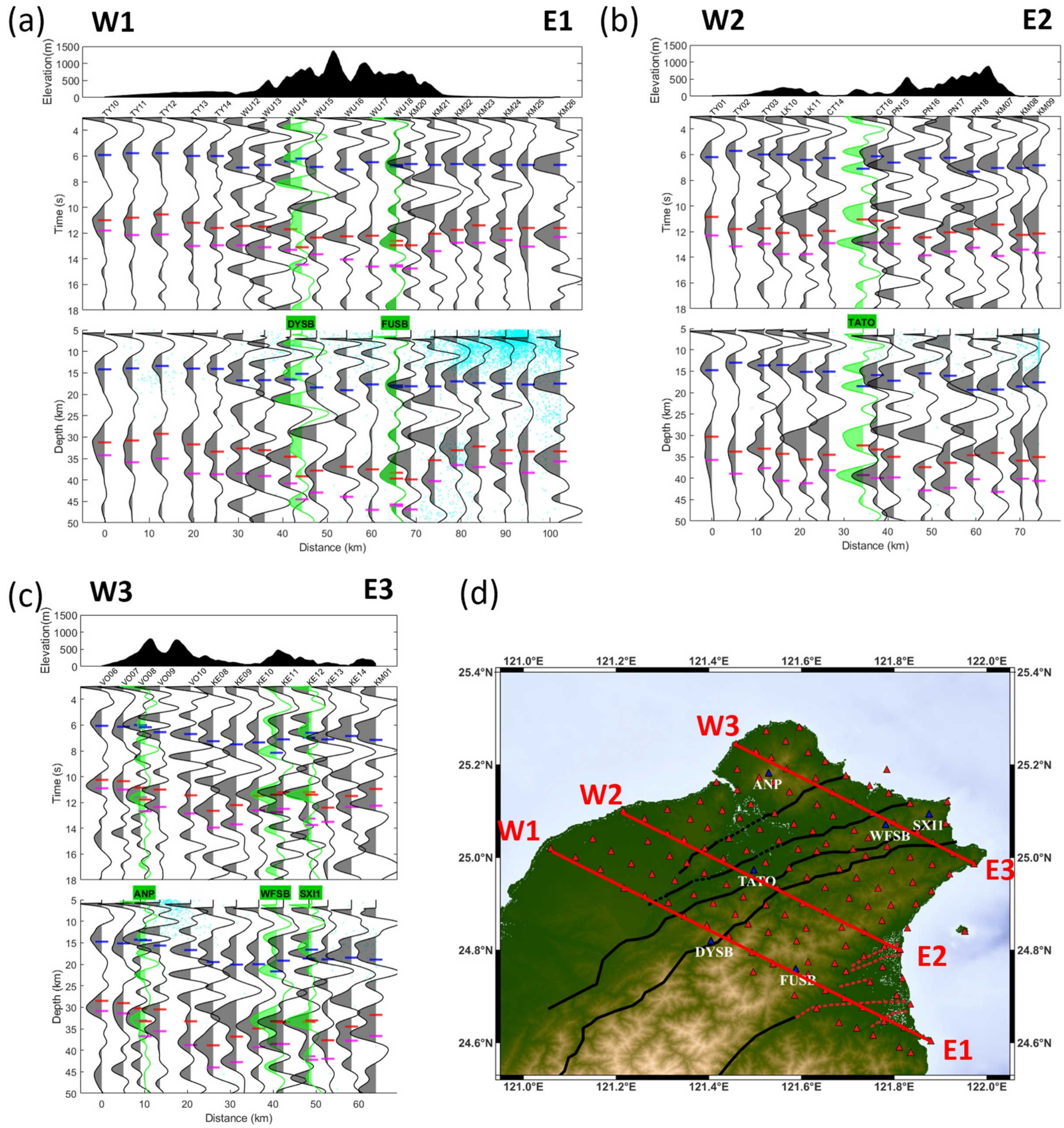

Figure 6. (a–c) Autocorrelation functions from the Formosa Array (black wiggle traces) shown alongside those from BATS and CWASN (green wiggle traces) across three profiles. Top panels: Surface topography along each profile. Middle panels: Autocorrelation functions along the profiles in two-way travel time. Bottom panels: Depth-converted autocorrelation functions from the middle panels. Cyan circles represent earthquakes projected within 2.5 km of the profile. Tick marks denote the interpreted reflectors: Moho (magenta), Reflector 1 (red), and Reflector 2 (blue). (d) Black lines show fault traces (same as Figure 1b); red triangles denote Formosa Array stations; and blue triangles denote BATS and CWASN stations.

To better approximate the effective wavelet of our processed ACFs, we repeat the calculations using a data-derived, zero-phase source spectrum estimated from short windows around the observed reflection arrivals (Text S5 in Supporting Information S1; Figure 9c). Using a data-derived wavelet produces synthetic seismograms more closely resembling our observed ACFs.

As an additional sensitivity test, we explored a model that includes a low-velocity layer immediately above the 15-km interface (Reflector 2) to evaluate how reduced upper-crustal velocities affect wave-packet shape and reverberation interference. The resulting synthetics show increased reverberatory complexity and broader troughs

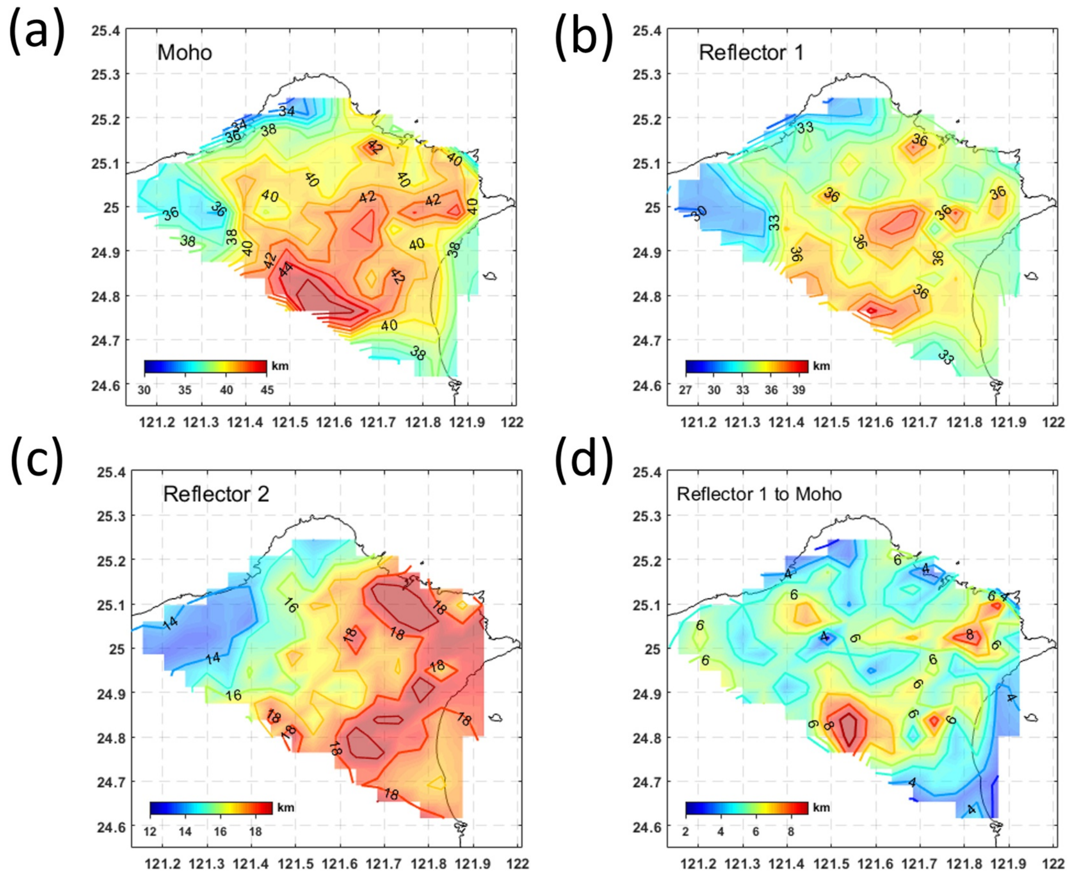

Figure 7. Depth to (a) the Moho, (b) Reflector 1, and (c) Reflector 2. (d) Thickness between Reflector 1 and the Moho.

in the Reflector-2 time window (Figure S2 in Supporting Information S1). This end-member test illustrates that the Reflector-2 wave packet is sensitive to plausible velocity variations in the overlying section and that a broad (and occasionally split) signal can arise from interference between the 15-km primary reflection and shallow reverberations.

Because these tests assume a 1-D, horizontally layered medium and vertical incidence, they are intended to evaluate the timing of primary reflections and multiples and the effects of interference, rather than for direct interpretation of the data. In 3-D settings, heterogeneity and dip can shift times, alter polarity and amplitude, and introduce additional scattering. Nevertheless, the synthetics are useful for identifying lag-time windows susceptible to overlap between primary reflections and shallow reverberations and for examining wavelet stretch from time-to-depth conversion.

4. Discussion

We first compare the ACF-derived Moho geometry with independent constraints (Section 4.1). We then discuss the origin of the Moho-parallel Reflector 1 band (Section 4.2) and the tectonic significance of the dipping Reflector 2 interface (Section 4.3). Finally, we integrate these observations into a conceptual tectonic model for northern Taiwan (Section 4.4) and consider the implications for regional deformation style (Section 4.5).

4.1. Moho Geometry and Crustal Thickness in Northern Taiwan

Our ACF-derived Moho depths show a coherent regional pattern of crustal thickening beneath the mountain belt and crustal thinning toward the Ilan Plain. This geometry is broadly consistent with independent constraints reported in previous studies. The southernmost Formosa Array profile lies close to the TAIGER T6 wide-angle refraction profile; both data sets show Moho deepening beneath the Hsueshan Range and reaching ∼40 km

10.1029/2025JB033147

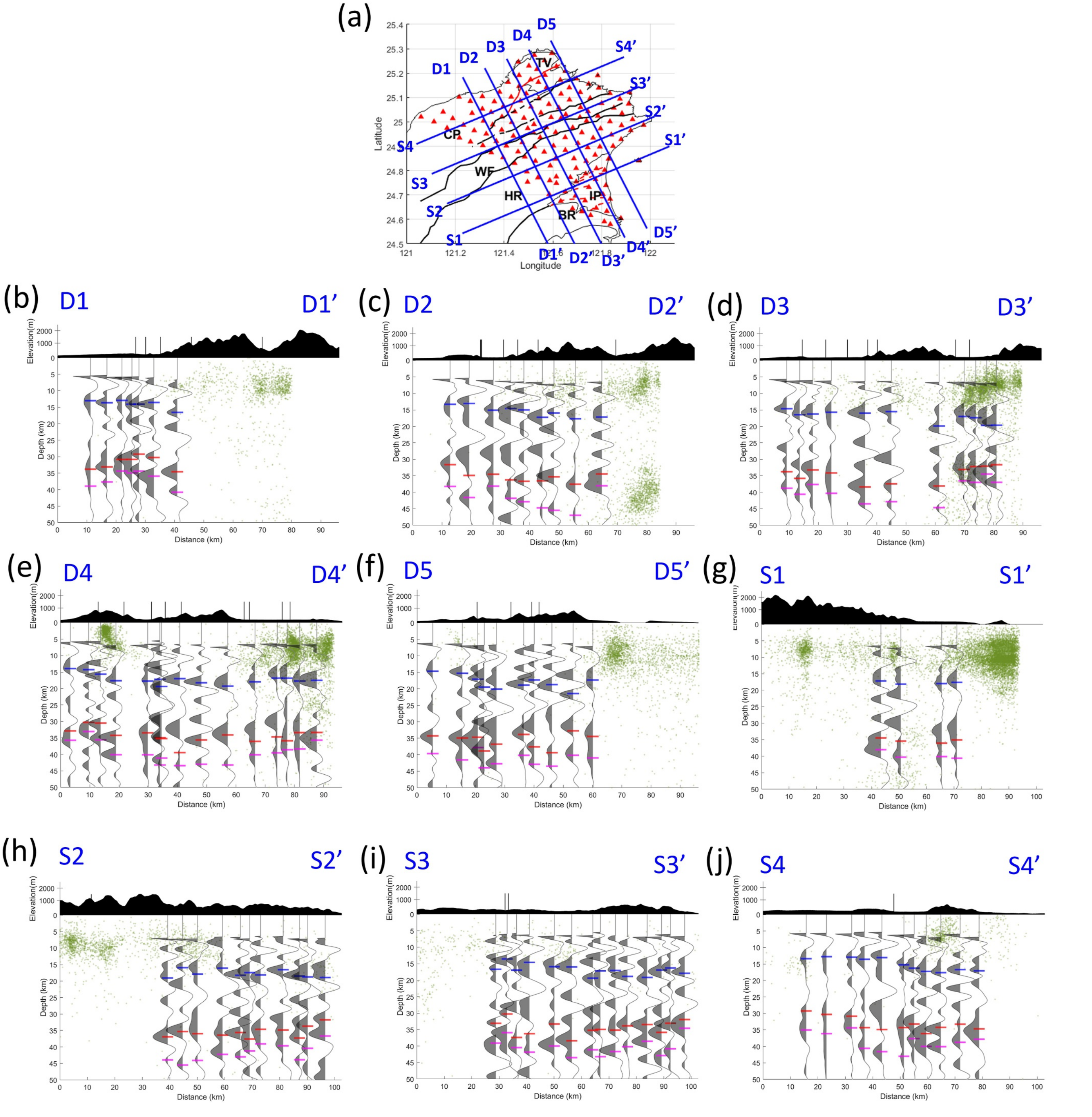

Figure 8. (a) Map showing the locations of the cross-section profiles (blue) and stations (red triangles). Profiles include five dip-oriented lines (D1–D1′ to D5–D5′) and four strike-oriented lines (S1–S1′ to S4–S4′). (b–j) Along-profile autocorrelation functions (wiggle traces) plotted versus distance for stations located within 2.5 km of each profile trace, with surface topography shown as the black filled curve. Green dots show earthquakes within 2.5 km of the profile trace, projected onto the section. Colored picks mark interpreted reflector depths: Moho (magenta), Reflector 1 (red), and Reflector 2 (blue).

beneath the Central Range (Van Avendonk et al., 2016). A gravity inversion constrained by seismic observations similarly indicates crustal thickening beneath the mountainous region, consistent with the along-strike trend shown by our Moho map in Figure 7a (Hsieh & Yen, 2016). Receiver-function CCP images from TAIGER data also show strong Moho Ps energy at ~30–40 km that deepens beneath the mountains (Chi et al., 2022), in agreement with the first-order structure we infer from autocorrelation.

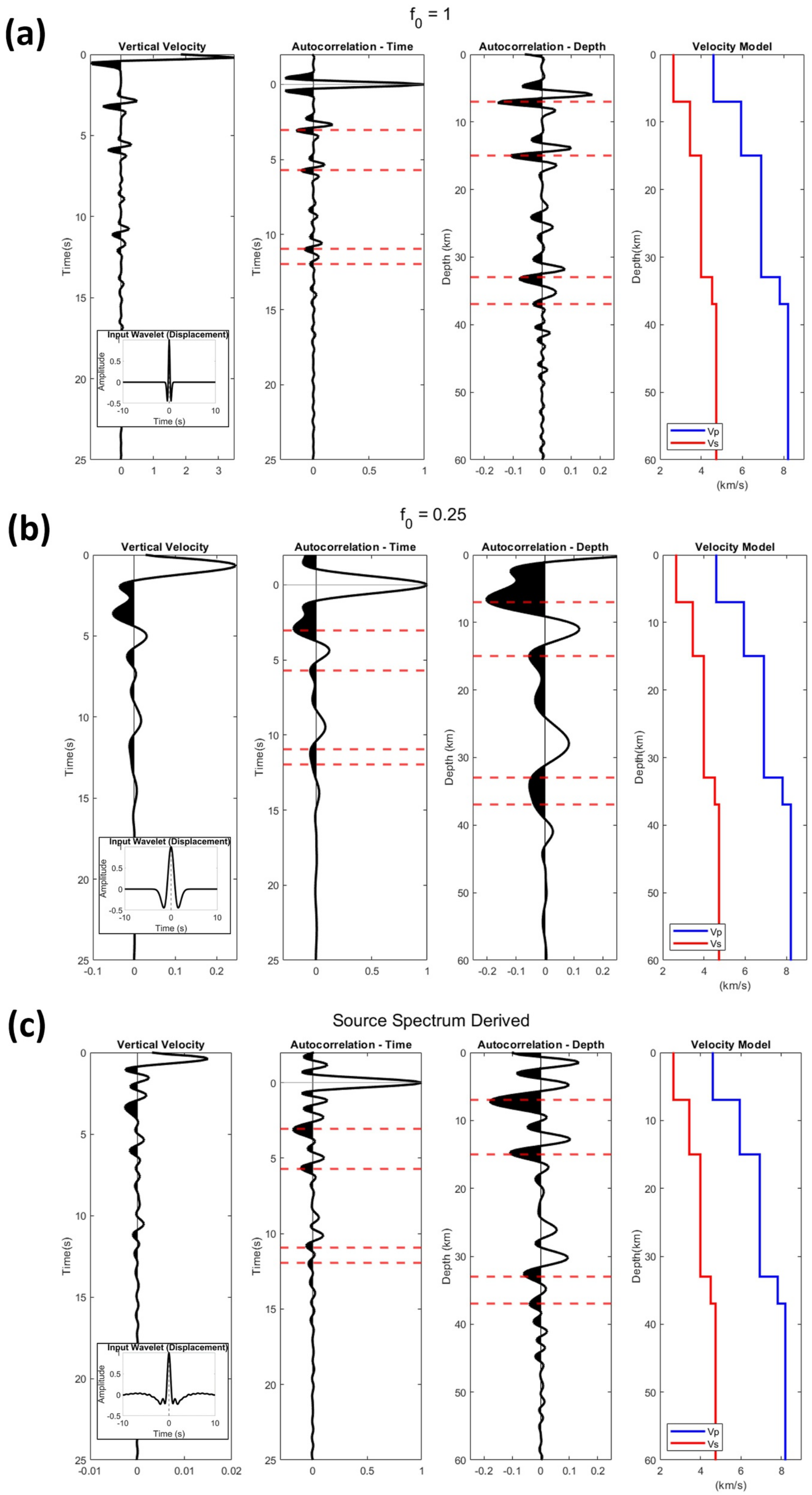
(a)
f_0 = 1
Vertical Velocity
Autocorrelation - Time
Autocorrelation - Depth
Velocity Model
Input Wavelet (Displacement)
Time(s)
Depth (km)
Vp
Vs
(km/s)
(b)
f_0 = 0.25
(c)
Source Spectrum Derived

Figure 9.

Differences among published Moho depths partly reflect methodological differences and differences in resolution. Autocorrelation reflectivity is sensitive to sharp impedance contrasts at well-defined velocity boundaries. Thus, ACF-derived picks need not coincide with a specific tomographic contour; instead, they are expected to fall within the depth interval where velocity increases most rapidly. In regional earthquake tomography of Taiwan, the Moho is often defined as a velocity contour, Vp = 7.5 km/s, representing a gradual transition from crust to mantle velocities rather than a discrete impedance jump (Huang et al., 2014; Kuo-Chen et al., 2012). Ai et al. (2019) identified the strongest Vs gradient in their ambient noise Rayleigh wave tomography model as a Moho proxy. Their model yields comparable Moho depths (~30–45 km) across Taiwan and offshore, consistent with our Moho estimates.

Receiver function studies in our study area relied primarily on BATS stations (Chi et al., 2022; Goyal & Hung, 2021; Kim et al., 2004; Wang et al., 2010). In our sections, the five BATS stations and one CWASN station show Moho depths between 30 and 40 km, with patterns similar to nearby Formosa Array stations (Figure 6), indicating consistency across networks. Kim et al. (2004), with only one station (TATO) within our study area, estimated a Moho depth of ~30–36 km beneath the Taipei region, while our ACF estimate at TATO is ~38 km. In contrast, Wang et al. (2010) and Goyal and Hung (2021) reported locally shallower Moho estimates (~18–24 km) at the northern edge of Taiwan, >12 km shallower than our ACF depths (~36 km). In our ACF sections, adjacent inland stations show a laterally coherent late-time negative event which we interpret as the Moho, whereas the northern coastal profile exhibits sustained reverberations between Reflector 2 and the deepest event that reduce our confidence in Moho identification. We therefore treat Moho picks along the immediate coast as lower confidence and emphasize the regional Moho trend defined primarily by the inland array.

Finally, the relatively shallow Moho beneath the Ilan Plain is consistent with the broader tectonic setting near the western termination of the Okinawa Trough. The Ilan Plain is commonly considered the southwestward continuation of the Okinawa back-arc system, and extension associated with back-arc opening provides a plausible explanation for the relatively thin crust there.

4.2. Interpretation of Reflector 1

Reflector 1 is a laterally coherent band of negative reflection amplitude (positive polarity events) immediately above the Moho arrival, giving a lower crustal layer with a thickness of ~2–10 km (Figures 6 and 7d). Receiver-function CCP images along the TAIGER northern east–west transect, located just south of the Formosa Array, independently show a high-amplitude lowermost-crustal band of comparable thickness (~8 km), supporting a regionally coherent layer at the base of the crust (Chi et al., 2022).

We interpret Reflector 1 as a mafic underplated layer at the base of the crust. Magmatic underplating commonly produces subhorizontal, high-amplitude reflectors at the base of the crust and is associated with high seismic velocities and densities (Thybo & Artemieva, 2013). Where published velocity and density models overlap our profiles, Reflector 1 lies within a high-velocity, high-density lowermost crustal interval. In Huang et al. (2014), Reflector 1 falls between the Vp = 7.0 and 7.5 km/s contours. In Kuo-Chen et al. (2012), it falls between the Vp = 7.5 and 8 km/s contours. In the gravity model, it coincides with ~3.1–3.3 g/cm^3 density contours from Hsieh and Yen (2016). These values are consistent with mafic lower-crustal lithologies such as mafic granulite or gabbro (Christensen & Mooney, 1995; Christensen & Salisbury, 1975).

Previous work has linked lower-crustal magmatism in northern Taiwan to slab rollback and Okinawa Trough opening, or to post-collisional delamination (Teng, 1996; Teng et al., 2000; Wang et al., 1999). However, these processes are commonly tied to localized, geologically young volcanism in the Northern Taiwan Volcanic Zone, and available geophysical images suggest spatially patchy lower-crustal additions rather than a broad Moho-

Figure 9. Haskell propagator-matrix synthetics for a vertically incident plane-wave in a 1-D layered reference model and the resulting autocorrelations. All panels use the same five-layer velocity structure with interfaces at depths of 7, 15, 33, and 37 km (a shallow reflector, Reflector 2, Reflector 1, and the Moho). Each panel shows the vertical-component velocity synthetic seismogram, the autocorrelation in time lag, and the depth-converted autocorrelation. The source wavelet is applied to the displacement response and the result is differentiated to obtain velocity; the inset shows the input displacement wavelet. Source wavelets are Ricker with central frequency $f_0 = 1$ Hz in (a) and $f_0 = 0.25$ Hz in (b), and an empirical zero-phase spectrum estimated from the observed stacked ACF spectrum in (c). Red dashed lines mark the predicted two-way travel times of PP reflections and corresponding depths to each interface.

10.1029/2025JB033147

parallel layer (e.g., Huang et al., 2021). We therefore suggest that rollback- or delamination-related magmatism may overprint the lower crust locally but is unlikely to be the primary cause of laterally persistent Reflector 1 mapped here.

A plausible explanation for the pervasive, Moho-parallel Reflector 1 is that it represents high-velocity lower crust emplaced during South China Sea Plate (SCS) rifting that has been subsequently incorporated into the Taiwan orogen. Along the northern SCS margin, wide-angle refraction studies have imaged high-velocity lower crust (HVLC) with Vp > 7.0 km/s and thicknesses of a few to ∼10 km (e.g., Lester et al., 2014; Sun et al., 2019; Zhang, Zhao, Ding, et al., 2023; Zhang, Zhao, Sun, et al., 2023), comparable to the thickness and inferred velocity range associated with Reflector 1. Proposed timing and generation mechanisms vary across the margin and include, among others, pre-rift arc-related subduction magmatism, syn-rift decompression melting, late syn-rift to early-spreading magmatic upwelling, and post-spreading magmatism (Sun et al., 2019; Wan et al., 2017; Wei et al., 2011; Zhang, Zhao, Ding, et al., 2023; Zhang, Zhao, Sun, et al., 2023). Because SCS rifting predates Taiwan collision and the subsequent subduction polarity flip, such underplating could have been laterally extensive along the margin. This layer was later transported into the orogen and thickened while remaining broadly Moho-parallel. This inheritance model provides a straightforward explanation for the continuity of Reflector 1 across our profiles and its variable thickness. Comparable HVLC underplating is reported at volcanic passive margins worldwide, including East Greenland and the Vøring Margin (Abdelmalak et al., 2017; Voss & Jokat, 2007). A further analog is the GUMBO wide-angle profiles in the northern Gulf of Mexico, where rifting generated a several-kilometer-thick HVLC layer (Vp > 7.2 km/s) at the base of stretched continental crust, interpreted as decompression-melting underplating near the Moho (Eddy et al., 2014). The widespread occurrence of HVLC along the SCS margin therefore lends support to underplating as a simpler explanation for Reflector 1.

4.3. Interpretation of Reflector 2

Reflector 2 is a laterally continuous intracrustal reflector at ∼12–22 km depth that dips ∼3°–7° to the east–southeast (Figures 7c and 8). Seismicity is predominantly located above Reflector 2 (Figure 8), and several profiles show intermittent shallow reflectivity at ∼4–10 km depth above it.

Intracrustal boundaries at similar depths have been reported in previous studies. Receiver-function results along an east–west TAIGER profile identify a boundary at ∼15–20 km depth that was interpreted as a rheological transition zone, above which most earthquakes occur. However, a brittle–ductile transition is not necessarily reflective unless it coincides with a sharp impedance contrast. Kim et al. (2004) also inferred a mid-crustal velocity jump near ∼18–20 km and proposed a Conrad discontinuity, marking a compositional change from felsic upper crust to more mafic lower crust. While these interpretations can explain a mid-crustal boundary, they do not by themselves predict a regionally continuous, gently dipping surface with the observed seismicity partitioning. Depth-dependent deformation has also been inferred from crustal anisotropy (Huang et al., 2015), but that signal weakens toward northern Taiwan and does not uniquely constrain a single dipping interface.

Based on its depth, east–southeastward dip, lateral continuity, and the predominance of earthquakes above it, we interpret Reflector 2 as an eastward-dipping detachment surface, consistent with thin-skinned models for Taiwan that place the detachment at ∼10–20 km depth with a gentle ∼5–6° dip (Suppe, 1981). In this geometry, the detachment dips eastward beneath the west-verging fold-and-thrust belt, consistent with a basal décollement that decouples deformation in the upper-crustal wedge from the underlying crust. The intermittent shallow reflectivity above Reflector 2 may reflect imbricate thrusts or back-thrusts within the wedge. Consistent with this interpretation, ACF waveforms become more complex beneath the Western Foothills and Hsueshan Range, where multiple pulses are observed (Figures 6 and 8), indicating increased structural complexity above the detachment.

4.4. Conceptual Tectonic Model

Figure 10 synthesizes the key reflectivity features imaged by the Formosa Array autocorrelation functions into a conceptual model for northern Taiwan. The ACF sections show three first-order elements: (a) a Moho that deepens beneath the mountain belt and shallows toward the Ilan Plain, (b) a laterally continuous, but variably thick, Moho-parallel reflective band in the lowermost crust (Reflector 1), and (c) a gently east-dipping intracrustal interface at ∼12–20 km depth (Reflector 2), above which seismicity is concentrated.

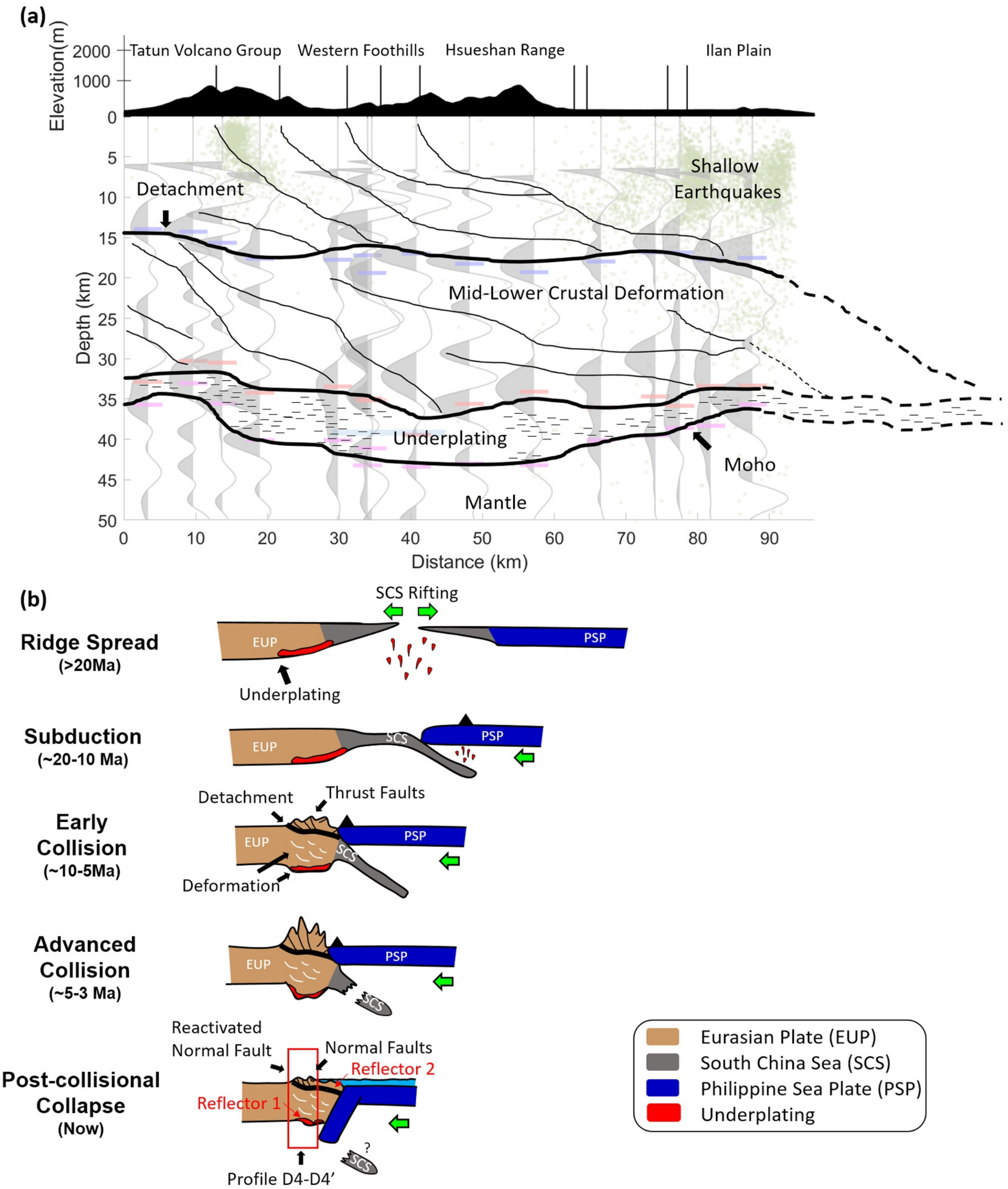

Figure 10. (a) Geological interpretation of profile D4–D4' (see Figure 8), based on autocorrelation functions. Vertical black lines on the topography profile mark the locations of surface fault traces. (b) Schematic diagram of the tectonic evolution of Taiwan. Green arrows indicate relative plate-motion directions. Black triangles mark surface volcanism. Black lines and white lines within the mountains denote folds, faults, and deformation structures.

In the interpretation shown in Figure 10a, Reflector 2 marks a basal detachment that decouples upper-crustal deformation from deeper crustal processes. The fold-and-thrust structures and intermittent shallow reflectivity are concentrated above this surface, whereas reflectivity below it is more discontinuous, consistent with distributed deformation in the middle to lower crust. Reflector 1 is interpreted as an inherited high-velocity lower-crustal layer emplaced prior to collision (e.g., rift-related underplating along the South China Sea margin) and later incorporated into the orogen while remaining broadly Moho-parallel.

Figure 10b summarizes the inferred tectonic evolution. Prior to collision, rifting of the South China Sea margin generated a thinned continental crust with an underplated lower-crustal layer. With northwestward motion of the Philippine Sea Plate, subduction initiated and arc magmatism developed. Collision began in southern Taiwan at

~6 Ma and progressively propagated northward, producing upper-crustal shortening above the detachment, crustal thickening, and modification of inherited lower-crustal structure. In northern Taiwan, collision has since waned, and post-collisional extension associated with the western termination of the Okinawa Trough has contributed to crustal thinning beneath the Ilan Plain. The observed detachment, lower-crustal reflectivity, and Moho geometry thus collectively record both inherited rift structure and subsequent collision-related deformation.

4.5. Implications for Deformation Style

The imaging of a laterally continuous detachment surface (Reflector 2) raises the question of whether deformation in northern Taiwan is primarily thin-skinned. In thin-skinned systems, seismicity is commonly concentrated near and above the basal detachment, with fewer events below where deformation is limited or more distributed (Camanni et al., 2014; Carena et al., 2002; Dahlen et al., 1984; Davis et al., 1983; Ni & Barazangi, 1984). In our study area, earthquakes are predominantly located above Reflector 2, with additional clustering along normal faults beneath the Ilan Plain (Figures 6a, 8, and 10a). This distribution is consistent with Reflector 2 mechanically decoupling brittle deformation in the upper crust from weaker or more distributed deformation below. Events that plot well below Reflector 2 occur mainly toward the eastern side of the study area and likely include subduction-related earthquakes within the Philippine Sea Plate, so they are not expected to track an upper-plate detachment surface.

At the same time, our ACF images indicate that deformation in northern Taiwan is not purely thin-skinned. Beneath Reflector 2, the lower-crustal signals are complex and discontinuous, and several deeper arrivals share an eastward-dipping tendency broadly consistent with the detachment geometry (Figures 6, 8, and 10a). This suggests that the middle to lower crust has experienced distributed deformation and localized shear, even if most brittle faulting and seismicity are concentrated above Reflector 2. The thin-skinned model alone (Suppe, 1981) therefore does not fully explain the observed crustal structure. Instead, the data support vertically partitioned deformation, in which upper-crustal faulting is decoupled from deeper crustal deformation but remains mechanically linked through inherited structure and rheological layering.

Comparisons with central Taiwan and observations farther south reinforce this interpretation. In central Taiwan, magnetotelluric and seismicity studies indicate that steeply dipping faults penetrate into the middle to lower crust, disrupt the basal detachment, and involve much of the crustal column (Bertrand et al., 2012; Brown et al., 2012; Gourley et al., 2007; Kaus et al., 2008; Mouthereau & Lacombe, 2006; Wu et al., 1997; Yamato et al., 2009). Constraints from crustal anisotropy have likewise been interpreted to reflect depth-dependent deformation in central and southern Taiwan, whereas the anisotropic signal in northern Taiwan weakens at greater depth (Huang et al., 2015). These differences suggest that deformation style varies from north to south: northern Taiwan shows stronger upper-crustal decoupling above a mid-crustal detachment, while central Taiwan exhibits more pervasive crustal involvement.

This partitioned structure is consistent with the tectonic evolution outlined in Section 4.4. In northern Taiwan, collision has waned and post-collisional extension related to the western termination of the Okinawa Trough is active, yet detachment-level and deeper inherited structures can persist as rheological boundaries and zones of localized damage. Such inherited interfaces may remain reflective and continue to influence where strain and seismicity localize, preserving a record of earlier collision-related deformation even as the present-day stress regime evolves.

If this interpretation is correct, similar detachment surfaces and lowermost-crustal reflective bands may also occur farther south where collision is ongoing, but their geometry, reflectivity, and associated seismic expression should vary systematically along the north–south trend of the Taiwan orogen. Specifically, areas closer to the active collision front may show stronger crustal thickening and more pervasive deep deformation, whereas regions transitioning into post-collisional extension should exhibit greater upper-crustal decoupling and enhanced normal faulting. Ambient-noise autocorrelation imaging provides a promising means of testing this hypothesis and tracking how deformation style evolves along the Taiwan orogen.

10.1029/2025JB033147

5. Conclusions

Using Formosa Array data, ambient noise autocorrelation reveals three laterally persistent reflectors beneath northern Taiwan: the Moho at ∼30–47 km depth, a Moho-parallel lowermost-crustal band (Reflector 1) a few kilometers above it, and a gently east–southeast dipping mid-crustal interface (Reflector 2) at ∼12–20 km depth. The Moho deepens beneath the mountain belt and shallows toward the Ilan Plain, consistent with independent refraction, gravity, and receiver-function constraints. Reflector 1 is best explained as an inherited high-velocity lower-crustal layer, plausibly related to rift-era underplating along the South China Sea margin and later incorporated into the orogeny. Reflector 2 aligns with increased waveform complexity and a strong partitioning of seismicity above the interface, supporting interpretation as a regional detachment that decouples brittle upper-crustal deformation from deeper crustal processes. Synthetic and uncertainty tests indicate that the main arrivals are robust and that depth uncertainties are modest (∼1–2 km for intracrustal phases; slightly larger for the Moho). The results support vertically partitioned deformation in northern Taiwan, with thin-skinned behavior above a mid-crustal detachment together with inherited lower-crustal structure, and demonstrate the utility of dense-array autocorrelation for mapping crustal interfaces in active orogens.

Conflict of Interest

The authors declare no conflicts of interest relevant to this study.

Availability Statement

The processed data products generated in this study include station-stacked vertical-component autocorrelation functions, station-specific 1-D velocity models used for depth conversion, and reflector pick times. These products are archived in a curated repository (Chien et al., 2026).

The raw continuous waveforms from the Formosa Array are third-party data and are not redistributed by the authors; they remain available from the data owner under their access policies (Academia Sinica, Institute of Earth Sciences, 2017). Additional waveform data are available from BATS (Institute of Earth Sciences, Academia Sinica, 1996) and the IRIS/USGS Global Seismograph Network (Albuquerque Seismological Laboratory/USGS, 1988). Waveform and earthquake information from the Central Weather Administration are available via GDMS (Central Weather Administration, 2012). Autocorrelation processing was performed in MATLAB (MathWorks, 2023), and figures were produced in MATLAB and Python (Python Software Foundation, 2020).

Acknowledgments
We thank the data providers for access to waveform and earthquake data from the Formosa Array, BATS, the IRIS/USGS Global Seismograph Network (GSN), and the Central Weather Administration GDMS. We thank the editor and reviewers for their careful review and constructive feedback, which significantly improved the manuscript.

References

Abdelmalak, M. M., Faleide, J. I., Planke, S., Gernigon, L., Zastrozhnov, D., Shephard, G. E., & Myklebust, R. (2017). The T-reflection and the deep crustal structure of the Vøring margin, offshore mid-Norway. *Tectonics*, *36*(11), 2497–2523. https://doi.org/10.1002/2017TC004617

Ai, S., Zheng, Y., & Xiong, C. (2019). Ambient noise tomography across the Taiwan Strait, Taiwan Island, and Southwestern Ryukyu Arc: Implications for subsurface slab interactions. *Tectonics*, *38*(2), 579–594. https://doi.org/10.1029/2018TC005355

Aki, K., & Richards, P. G. (1980). *Quantitative seismology: Theory and methods* (Vol. 2, p. 930). W. H. Freeman.

Albuquerque Seismological Laboratory/USGS. (1988). Global Seismograph Network (GSN—IRIS/USGS) [Dataset]. *International Federation of Digital Seismograph Networks*. https://doi.org/10.7914/SN/IU

Alemayehu, S., Aoudia, A., Ayele, A., Pachhai, S., Thapa, H. R., Ebinger, C. J., et al. (2023). Structure of the crust-uppermost mantle beneath the Ethiopian volcanic province using ambient seismic noise and teleseismic P wave coda autocorrelation. *Tectonophysics*, *869*, 230092. https://doi.org/10.1016/j.tecto.2023.230092

Ammon, C. J. (1991). The isolation of receiver effects from teleseismic P waveforms. *Bulletin of the Seismological Society of America*, *81*(6), 2504–2510. https://doi.org/10.1785/BSSA0810062504

Ashruf, T. N., & Morelli, A. (2022). The Moho reflectivity of the subduction beneath the Southwestern Alps from ambient seismic noise autocorrelations. *Geophysical Journal International*, *230*(1), 298–316. https://doi.org/10.1093/gji/ggac079

Bensen, G. D., Ritzwoller, M. H., Barmin, M. P., Levshin, A. L., Lin, F., Moschetti, M. P., et al. (2007). Processing seismic ambient noise data to obtain reliable broad-band surface wave dispersion measurements. *Geophysical Journal International*, *169*(3), 1239–1260. https://doi.org/10.1111/j.1365-246X.2007.03374.x

Bertrand, E. A., Unsworth, M. J., Chiang, C.-W., Chen, C.-S., Chen, C.-C., Wu, F. T., et al. (2012). Magnetotelluric imaging beneath the Taiwan orogen: An arc-continent collision. *Journal of Geophysical Research*, *117*(B1), B01402. https://doi.org/10.1029/2011JB008688

Brown, D., Alvarez-Marron, J., Schimmel, M., Wu, Y., & Camanni, G. (2012). The structure and kinematics of the central Taiwan mountain belt derived from geological and seismicity data. *Tectonics*, *31*(5), TC5013. https://doi.org/10.1029/2012TC003156

Camanni, G., Chen, C. H., Brown, D., Alvarez-Marron, J., Wu, Y. M., Chen, H. A., et al. (2014). Basin inversion in central Taiwan and its importance for seismic hazard. *Geology*, *42*(2), 147–150. https://doi.org/10.1130/G35102.1

Carena, S., Suppe, J., & Kao, H. (2002). Active detachment of Taiwan illuminated by small earthquakes and its control of first-order topography. *Geology*, *30*(10), 935. https://doi.org/10.1130/0091-7613(2002)030<0935:ADOTIB>2.0.CO;2

Central Weather Administration (CWA, Taiwan). (2012). Central Weather Administration Seismographic Network [Dataset]. *International Federation of Digital Seismograph Networks*. https://doi.org/10.7914/SN/T5

Chi, T. C., Chang, Y. F., & Huang, B. S. (2022). Receiver function imaging of the crustal structure beneath northern Taiwan using dense linear arrays. *Geosciences*, *12*(3), 136. https://doi.org/10.3390/geosciences12030136

Chien, M., Levander, A., & Chen, P.-F. (submitted). Seismic noise recorded by the Formosa array.

Chien, M., Levander, A., & Chen, P.-F. (2026). Replication data for: Autocorrelation seismic imaging of northern Taiwan using ambient noise data [Dataset]. *Harvard Dataverse*. https://doi.org/10.7910/DVN/B262MK

Christensen, N. I., & Salisbury, M. H. (1975). Structure and constitution of the lower oceanic crust. *Reviews of Geophysics*, *13*(1), 57–86. https://doi.org/10.1029/RG013i001p00057

Christensen, N. I., & Mooney, W. D. (1995). Seismic velocity structure and composition of the continental crust: A global view. *Journal of Geophysical Research*, *100*(B6), 9761–9788. https://doi.org/10.1029/95JB00259

Claerbout, J. F. (1968). Synthesis of a layered medium from its acoustic transmission response. *Geophysics*, *33*(2), 264–269. https://doi.org/10.1190/1.1439927

Dahlen, F. A., Suppe, J., & Davis, D. (1984). Mechanics of fold-and-thrust belts and accretionary wedges: Cohesive Coulomb theory. *Journal of Geophysical Research*, *89*(B12), 10087–10101. https://doi.org/10.1029/JB089iB12p10087

Davis, D., Suppe, J., & Dahlen, F. A. (1983). Mechanics of fold-and- thrust belts and accretionary wedges. *Journal of Geophysical Research*, *88*(B2), 1153–1172. https://doi.org/10.1029/JB088iB02p01153

Deng, S., & Levander, A. (2020). Autocorrelation reflectivity of Mars. *Geophysical Research Letters*, *47*(16), e2020GL089630. https://doi.org/10.1029/2020GL089630

Deng, S., & Levander, A. (2023). Seismic autocorrelation analysis of deep Mars. *Geophysical Research Letters*, *50*(24), e2023GL105046. https://doi.org/10.1029/2023GL105046

Eddy, D. R., Van Avendonk, H. J. A., Christeson, G. L., Norton, I. O., Karner, G. D., Johnson, C. A., & Snedden, J. W. (2014). Deep crustal structure of the northeastern Gulf of Mexico: Implications for rift evolution and seafloor spreading. *Journal of Geophysical Research: Solid Earth*, *119*(9), 6802–6822. https://doi.org/10.1002/2014JB011311

Frasier, C. W. (1970). Discrete time solution of plane P-SV waves in a plane layered medium. *Geophysics*, *35*(2), 197–219. https://doi.org/10.1190/1.1440085

Gardner, G. H. F., Gardner, L. W., & Gregory, A. R. (1974). Formation velocity and density; the diagnostic basics for stratigraphic traps. *Geophysics*, *39*(6), 770–780. https://doi.org/10.1190/1.1440465

Gómez-García, C., Lebedev, S., Meier, T., Xu, Y., Le Pape, F., & Wiesenberg, L. (2023). Ambient noise autocorrelation scheme for imaging the P-wave reflectivity of the lithosphere. *Geophysical Journal International*, *233*(3), 1671–1693. https://doi.org/10.1093/gji/ggac509

Gorbatov, A., Saygin, E., & Kennett, B. L. N. (2013). Crustal properties from seismic station autocorrelograms. *Geophysical Journal International*, *192*(2), 861–870. https://doi.org/10.1093/gji/ggs064

Gourley, J. R., Byrne, T., Chan, Y.-C., Wu, F., & Rau, R.-J. (2007). Fault geometries illuminated from seismicity in central Taiwan: Implications for crustal scale structural boundaries in the northern Central Range. *Tectonophysics*, *445*(3), 168–185. https://doi.org/10.1016/j.tecto.2007.08.013

Goyal, A., & Hung, S. H. (2021). Lateral variations of Moho depth and average crustal properties across the Taiwan orogen from H-V stacking of P and S receiver functions. *Geochemistry, Geophysics, Geosystems*, *22*(3), e2020GC009527. https://doi.org/10.1029/2020GC009527

Heath, B. A., Hooft, E. E. E., & Toomey, D. R. (2018). Autocorrelation of the seismic wavefield at Newberry volcano: Reflections from the magmatic and geothermal systems. *Geophysical Research Letters*, *45*(5), 2311–2318. https://doi.org/10.1002/2017GL076706

Ho, C. S. (1986). A synthesis of the geologic evolution of Taiwan. *Tectonophysics*, *125*(1–3), 1–16. https://doi.org/10.1016/0040-1951(86)90004-1

Hsieh, H.-H., & Yen, H.-Y. (2016). Three-dimensional density structures of Taiwan and tectonic implications based on the analysis of gravity data. *Journal of Asian Earth Sciences*, *124*, 247–259. https://doi.org/10.1016/j.jseaes.2016.05.009

Huang, H. H., Wu, Y. M., Song, X., Chang, C. H., Lee, S. J., Chang, T. M., & Hsieh, H. H. (2014). Joint Vp and Vs tomography of Taiwan: Implications for subduction-collision orogeny. *Earth and Planetary Science Letters*, *392*, 177–191. https://doi.org/10.1016/j.epsl.2014.02.026

Huang, H. H., Wu, E. S., Lin, C. H., Ko, J. Y. T., Shih, M. H., & Koulakov, I. (2021). Unveiling Tatun volcanic plumbing structure induced by post-collisional extension of Taiwan mountain belt. *Scientific Reports*, *11*(1), 5286. https://doi.org/10.1038/s41598-021-84763-z

Huang, T.-Y., Gung, Y., Kuo, B.-Y., Chiao, L.-Y., & Chen, Y.-N. (2015). Layered deformation in the Taiwan orogen. *Science*, *349*(6249), 720–723. https://doi.org/10.1126/science.aab1879

Institute of Earth Sciences, Academia Sinica, Taiwan. (1996). Broadband array in Taiwan for seismology [Dataset]. *International Federation of Digital Seismograph Networks*. https://doi.org/10.7914/SN/TW

Institute of Earth Sciences, Academia Sinica, Taiwan. (2017). Formosa array [Dataset]. *International Federation of Digital Seismograph Networks*. https://doi.org/10.7914/SN/FM

Ito, Y., Shiomi, K., Nakajima, J., & Hino, R. (2012). Autocorrelation analysis of ambient noise in northeastern Japan subduction zone. *Tectonophysics*, *572–573*, 38–46. https://doi.org/10.1016/j.tecto.2011.09.019

Kaus, B. J. P., Steedman, C., & Becker, T. W. (2008). From passive continental margin to mountain belt: Insights from analytical and numerical models and application to Taiwan. *Physics of the Earth and Planetary Interiors*, *171*(1), 235–251. https://doi.org/10.1016/j.pepi.2008.06.015

Kennett, B. L. N., Saygin, E., & Salmon, M. (2015). Stacking autocorrelograms to map Moho depth with high spatial resolution in southeastern Australia. *Geophysical Research Letters*, *42*(18), 7490–7497. https://doi.org/10.1002/2015GL065345

Kim, K. H., Chiu, J. M., Kao, H., Liu, Q., & Yeh, Y. H. (2004). A preliminary study of crustal structure in Taiwan region using receiver function analysis. *Geophysical Journal International*, *159*(1), 146–164. https://doi.org/10.1111/j.1365-246X.2004.02344.x

Kim, K. H., Chiu, J. M., Pujol, J., Chen, K. C., Huang, B. S., Yeh, Y. H., & Shen, P. (2005). Three-dimensional Vp and Vs structural models associated with the active subduction and collision tectonics in the Taiwan region. *Geophysical Journal International*, *162*(1), 204–220. https://doi.org/10.1111/j.1365-246X.2005.02657.x

Kuo, Y.-W., Wang, C.-Y., Kuo-Chen, H., Jin, X., Cai, H.-T., Lin, J.-Y., et al. (2016). Crustal structures from the Wuyi-Yunkai orogen to the Taiwan orogen: The onshore-offshore wide-angle seismic experiments of the TAIGER and ATSEE projects. *Tectonophysics*, *692*, 164–180. https://doi.org/10.1016/j.tecto.2015.09.014

Kuo-Chen, H., Wu, F. T., & Roecker, S. W. (2012). Three-dimensional P velocity structures of the lithosphere beneath Taiwan from the analysis of TAIGER and related seismic data sets. *Journal of Geophysical Research*, *117*(6), B06306. https://doi.org/10.1029/2011JB009108

Langston, C. A. (1979). Structure under Mount Rainier, Washington, inferred from teleseismic body waves. *Journal of Geophysical Research*, *84*(B9), 4749–4762. https://doi.org/10.1029/JB084iB09p04749

Lester, R., Van Avendonk, H. J. A., McIntosh, K., Lavier, L., Liu, C.-S., Wang, T. K., & Wu, F. (2014). Rifting and magmatism in the northeastern South China Sea from wide-angle tomography and seismic reflection imaging. *Journal of Geophysical Research: Solid Earth*, *119*(3), 2305–2323. https://doi.org/10.1002/2013JB010639

Lin, A. T., & Watts, A. B. (2002). Origin of the West Taiwan basin by orogenic loading and flexure of a rifted continental margin. *Journal of Geophysical Research*, *107*(B9), ETG2-1–19. https://doi.org/10.1029/2001jb000669

Lin, A. T., Watts, A. B., & Hesselbo, S. P. (2003). Cenozoic stratigraphy and subsidence history of the South China Sea margin in the Taiwan region. *Basin Research*, *15*(4), 453–478. https://doi.org/10.1046/j.1365-2117.2003.00215.x

Lin, J.-Y., Hsu, S.-K., Lin, A. T.-S., Yeh, Y.-C., & Lo, C.-L. (2016). Vp/Vs distribution in the northern Taiwan area: Implications for the tectonic structures and rock property variations. *Tectonophysics*, *692*, 181–190. https://doi.org/10.1016/j.tecto.2015.09.013

Liu, C. N., Lin, F. C., Huang, H. H., Wang, Y., Berg, E. M., & Lin, C. H. (2021). High-resolution 3-D shear wave velocity model of northern Taiwan via Bayesian joint inversion of Rayleigh wave ellipticity and phase velocity with Formosa array. *Journal of Geophysical Research: Solid Earth*, *126*(5), e2020JB021610. https://doi.org/10.1029/2020JB021610

MathWorks. (2023). MATLAB (version R2023a) [Software]. *The MathWorks, Inc*. Retrieved from https://www.mathworks.com

McIntosh, K., Nakamura, Y., Wang, T.-K., Shih, R.-C., Chen, A., & Liu, C.-S. (2005). Crustal-scale seismic profiles across Taiwan and the western Philippine Sea. *Tectonophysics*, *401*(1–2), 23–54. https://doi.org/10.1016/j.tecto.2005.02.015

Mouthereau, F., & Lacombe, O. (2006). Inversion of the Paleogene Chinese continental margin and thick-skinned deformation in the Western Foreland of Taiwan. *Journal of Structural Geology*, *28*(11), 1977–1993. https://doi.org/10.1016/j.jsg.2006.08.007

Nemcok, M., Mora, A., & Cosgrove, J. (2013). Thick-skin-dominated orogens; from initial inversion to full accretion: An introduction. *Geological Society of London Special Publications*, *377*, 1–17. https://doi.org/10.1144/SP377.17

Ni, J., & Barazangi, M. (1984). Seismotectonics of the Himalayan collision zone: Geometry of the underthrusting Indian plate beneath the Himalaya. *Journal of Geophysical Research*, *89*(B2), 1147–1163. https://doi.org/10.1029/JB089iB02p01147

Oren, C., & Nowack, R. L. (2017). Seismic body-wave interferometry using noise autocorrelations for crustal structure. *Geophysical Journal International*, *208*(1), 321–332. https://doi.org/10.1093/gji/ggw394

Ouammou, H., Aoudia, A., Javed, F., Ram Thapa, H., Tahayt, A., & Wang, H. (2026). The 2023 Mw 6.8 Al Haouz lower crustal earthquake buried in a thick crust within a thin lithosphere beneath the high atlas mountain range (morocco). *Seismological Research Letters*, *97*(2A), 730–742. https://doi.org/10.1785/0220250299

Phạm, T.-S., & Tkalčić, H. (2018). Antarctic ice properties revealed from teleseismic P wave coda autocorrelation. *Journal of Geophysical Research: Solid Earth*, *123*(9), 7896–7912. https://doi.org/10.1029/2018JB016115

Python Software Foundation. (2020). Python (version 3.8.8) [Software]. *Python Software Foundation*. Retrieved from https://www.python.org

Romero, P., & Schimmel, M. (2018). Mapping the basement of the Ebro basin in Spain with seismic ambient noise autocorrelations. *Journal of Geophysical Research: Solid Earth*, *123*(6), 5052–5067. https://doi.org/10.1029/2018JB015498

Schlunegger, F., & Kissling, E. (2015). Slab rollback orogeny in the Alps and evolution of the Swiss Molasse basin. *Nature Communications*, *6*(1), 8605. https://doi.org/10.1038/ncomms9605

Schuster, G. (2009). Reciprocity equations of convolution and correlation types. In G. T. Schuster (Ed.), *Seismic interferometry* (pp. 30–60). Cambridge University Press. https://doi.org/10.1017/CBO9780511581557.003

Sun, Z., Lin, J., Qiu, N., Jian, Z., Wang, P., Pang, X., et al. (2019). The role of magmatism in the thinning and breakup of the South China Sea continental margin: Special topic: The South China Sea Ocean Drilling. *National Science Review*, *6*(5), 871–876. https://doi.org/10.1093/nsr/nwz116

Suppe, J. (1981). Mechanics of mountain-building and metamorphism in Taiwan. *Geological Society of China*, (4), 67–89.

Suppe, J. (1984). Kinematics of arc-continent collision, flipping of subduction, and back-arc spreading near Taiwan. *Geological Society of China Memoir*, *6*, 131–146.

Teng, L. S. (1990). Geotectonic evolution of late Cenozoic arc-continent collision in Taiwan. *Tectonophysics*, *183*(1), 57–76. https://doi.org/10.1016/0040-1951(90)90188-E

Teng, L. S. (1996). Extensional collapse of the northern Taiwan mountain belt. *Geology*, *24*(10), 949–952. https://doi.org/10.1130/0091-7613(1996)024<0949:ECOTNT>2.3.CO;2

Teng, L. S., Lee, C. T., Tsai, Y. B., & Hsiao, L. Y. (2000). Slab breakoff as a mechanism for flipping of subduction polarity in Taiwan. *Geology*, *28*(2), 155–158. https://doi.org/10.1130/0091-7613(2000)28<155:SBAAMF>2.0.CO;2

Thapa, H. R., Pachhai, S., Aoudia, A., Manu-Marfo, D., Priestley, K., & Mitra, S. (2023). The Main Himalayan thrust beneath Nepal and southern Tibet illuminated by seismic ambient noise and teleseismic P wave coda autocorrelation. *Journal of Geophysical Research: Solid Earth*, *128*(8), e2022JB026195. https://doi.org/10.1029/2022JB026195

Thapa, H. R., & Vlahovic, G. (2025). High-resolution Moho depth and Vp/Vs mapping beneath the Carpatho–Pannonian region using P-wave coda autocorrelation. *Journal of Geophysical Research: Solid Earth*, *130*(5), e2024JB030491. https://doi.org/10.1029/2024JB030491

Thybo, H., & Artemieva, I. M. (2013). Moho and magmatic underplating in continental lithosphere. *Tectonophysics*, *609*, 605–619. https://doi.org/10.1016/j.tecto.2013.05.032

Tsai, M.-C., Yu, S.-B., Shin, T.-C., Kuo, K.-W., Leu, P.-L., Chang, C., & Ho, M.-Y. (2015). Velocity field derived from Taiwan continuous GPS array (2007–2013). *Terrestrial, Atmospheric and Oceanic Sciences*, *26*(5), 527. https://doi.org/10.3319/TAO.2015.05.21.01(T)

Ustaszewski, K., Wu, Y. M., Suppe, J., Huang, H. H., Chang, C. H., & Carena, S. (2012). Crust-mantle boundaries in the Taiwan-Luzon arc-continent collision system determined from local earthquake tomography and 1D models: Implications for the mode of subduction polarity reversal. *Tectonophysics*, *578*, 31–49. https://doi.org/10.1016/j.tecto.2011.12.029

Van Avendonk, H. J. A., McIntosh, K. D., Kuo-Chen, H., Lavier, L. L., Okaya, D. A., Wu, F. T., et al. (2016). A lithospheric profile across northern Taiwan: From arc-continent collision to extension. *Geophysical Journal International*, *204*(1), 331–346. https://doi.org/10.1093/gji/ggv468

Voss, M., & Jokat, W. (2007). Continent-ocean transition and voluminous magmatic underplating derived from P-wave velocity modelling of the East Greenland continental margin. *Geophysical Journal International*, *170*(2), 580–604. https://doi.org/10.1111/j.1365-246X.2007.03438.x

Wan, K., Xia, S., Cao, J., Sun, J., & Xu, H. (2017). Deep seismic structure of the northeastern South China Sea: Origin of a high-velocity layer in the lower crust. *Journal of Geophysical Research: Solid Earth*, *122*(4), 2831–2858. https://doi.org/10.1002/2016jb013481

Wang, H. L., Zhu, L., & Chen, H. W. (2010). Moho depth variation in Taiwan from teleseismic receiver functions. *Journal of Asian Earth Sciences*, *37*(3), 286–291. https://doi.org/10.1016/j.jseaes.2009.08.015

Wang, K.-L., Chung, S.-L., Chen, C.-H., Shinjo, R., Yang, T.-F., & Chen, C.-H. (1999). Post-collisional magmatism around northern Taiwan and its relation with opening of the Okinawa Trough. *Tectonophysics*, *308*(3), 363–376. https://doi.org/10.1016/S0040-1951(99)00111-0

Wapenaar, K., Draganov, D., Snieder, R., Campman, X., & Verdel, A. (2010). Tutorial on seismic interferometry: Part 1—Basic principles and applications. *Geophysics*, *75*(5), 75A195–75A209. https://doi.org/10.1190/1.3457445

Wapenaar, K., van der Neut, J., & Ruigrok, E. (2008). Passive seismic interferometry by multidimensional deconvolution. *Geophysics*, *73*(6), A51–A56. https://doi.org/10.1190/1.2976118

Wei, X.-D., Zhao, M., Ruan, A.-G., Qiu, X.-L., Hao, T.-Y., Wu, Z., et al. (2011). Crustal structure of shear waves and its tectonic significance in the mid-northern continental margin of the South China Sea. *Chinese Journal of Geophysics*, *54*, 3150–3160. https://doi.org/10.3969/j.issn.0001-5733,2011.12.015

Wissinger, E. S., Levander, A., Oldow, J., Fuis, G. S., & Lutter, W. (1998). Seismic profiling constraints on the evolution of the central Brooks Range, Arctic Alaska. *Special Papers - Geological Society of America*, *324*, 269–291. https://doi.org/10.1130/0-8137-2324-8.269

Wu, F. T., Kuo-Chen, H., & McIntosh, K. D. (2014). Subsurface imaging, TAIGER experiments and tectonic models of Taiwan. *Journal of Asian Earth Sciences*, *90*, 173–208. https://doi.org/10.1016/j.jseaes.2014.03.024

Wu, F. T., Rau, R.-J., & Salzberg, D. (1997). Taiwan orogeny: Thin-skinned or lithospheric collision? *Tectonophysics*, *274*(1), 191–220. https://doi.org/10.1016/S0040-1951(96)00304-6

Wu, Y. M., Chang, C. H., Zhao, L., Shyu, J. B. H., Chen, Y. G., Sieh, K., & Avouac, J. P. (2007). Seismic tomography of Taiwan: Improved constraints from a dense network of strong motion stations. *Journal of Geophysical Research*, *112*(8), B08312. https://doi.org/10.1029/2007JB004983

Wu, Y. M., Shyu, J. B. H., Chang, C. H., Zhao, L., Nakamura, M., & Hsu, S. K. (2009). Improved seismic tomography offshore northeastern Taiwan: Implications for subduction and collision processes between Taiwan and the southernmost Ryukyu. *Geophysical Journal International*, *178*(2), 1042–1054. https://doi.org/10.1111/j.1365-246X.2009.04180.x

Yamato, P., Mouthereau, F., & Burov, E. (2009). Taiwan mountain building: Insights from 2-D thermomechanical modelling of a rheologically stratified lithosphere. *Geophysical Journal International*, *176*(1), 307–326. https://doi.org/10.1111/j.1365-246X.2008.03977.x

Yu, S.-B., Chen, H.-Y., & Kuo, L.-C. (1997). Velocity field of GPS stations in the Taiwan area. *Tectonophysics*, *274*(1–3), 41–59. https://doi.org/10.1016/S0040-1951(96)00297-1

Zhang, J., Zhao, M., Ding, W., Ranero, C. R., Sallares, V., Gao, J., et al. (2023). New insights into the rift-to-drift process of the northern South China Sea margin constrained by a three-dimensional wide-angle seismic velocity model. *Journal of Geophysical Research: Solid Earth*, *128*(4), e2022JB026171. https://doi.org/10.1029/2022JB026171

Zhang, J., Zhao, M., Sun, Z., Sun, L., Xu, M., Yang, H., et al. (2023). Large volume of magma involved in South China Sea rifting: Implication for mantle breakup earlier than crust. *Tectonophysics*, *853*, 229801. https://doi.org/10.1016/j.tecto.2023.229801